# Advanced static speckle calibration for exo-planet imaging

Laurent Pueyo [a] Kent Wallace [a] Mitch Troy[a] Rick Burruss[a] Bruce Macintosh [b] and Remi Soummer [c]

(a) Jet propulsion Laboratory, California Institute of technology, 4800 Oak Grove Drive, Pasadena, CA 91109 , USA;
(b) Lawrence Livermore National Laboratory, Livermore, CA 94550 USA;
(c) Space Telescope Science Institute, 3700 San Martin Drive, Baltimore, MD 21218;

## ABSTRACT

In this communication we address the problem of post coronagraphic wavefront reconstruction. In high contrast imaging applications it is crucial to estimate the wavefront after the coronagraph, as close as possible to the science camera, in order to minimize non-common path errors. However closing the loop on such a measurement is a difficult exercise since several low order modes have been cancelled by the coronagraphs, thus leading to ill-posed inversion problems. Moreover sensing at the science detector is an intrusive method that disrupts the course of the observations. The Gemini Planet Imager (GPI) calibration system, based on a post-coronagraphic interferometer, provides an estimate of mid to high spatial frequencies aberrations that alleviates these two issues. However such a measurement have an intrinsic limitations that is related to the differential path errors between the two arm of the interferometer. In this paper we show how to devise wavefront reconstruction algorithms that account for these differential path errors. We identify two regimes, relative and absolute wavefront sensing, that depend on the magnitudes of the aberrations and the design of the coronagraph. We illustrate the performances for each regime. Finally we present experimental results obtained during the validation phase of show the results on laboratory data.

**Keywords:** exo-planets, coronagraphs, wavefront sensing

## 1. INTRODUCTION

Direct imaging of self luminous exo-planets will be possible in the near future from the ground using advanced instruments capable of delivering very high contrast Point Spread Functions (PSF) when imaging nearby stars. In instruments currently operating from ground based facilities the image of a point source exhibits a halo that is the superposition of two components. The first term is a smooth halo that corresponds to the the time average of the fast atmospheric residuals after Adaptive Optics (AO) correction.[1] Lowering the level of this halo with a few arc-seconds from the optical axis is a very active research area within the exo-planet imaging community,[2–4] whose intricacies are beyond the scope of the present communication. Here we focus on the second component of the post-coronagraphic halo, which is the granulated speckle field created by the time average of quasi-staic telescope and instrumental wavefront errors. Recent observations of the planetary system HR8799 showed the importance of measuring these errors and subtracting then using a Deformable Mirror (DM) before observation.[5] Such a calibration stage, also implemented in the SPHERE instrument,[6] lowers the absolute level of quasi-static speckles and assumes that they remain stable during the course of an observation. The architecture discussed here is an interferometric post-coronagraphic wavefront sensor which calibrates the quasi-static speckles in parallel with science exposures in addition to lowering their overall level. This ensures both absolute contrast and relative wavefront stability while observing a given source. Over the past few years, several authors have proposed to use interferences to retrieve the phase of light waves after coronagraphs[7] and discriminate between telescope artifacts and true astronomical companions.[8] The focus of this paper is on the calibration interferometer of the Gemini Planet Imager instrument (GPI), a solution proposed first by Wallace et.al.[9]

Further author information: (Send correspondence to Laurent Pueyo)
Laurent Pueyo.: E-mail: lpueyo@jpl.nasa.gov, Telephone: 1 818 354 3811

Adaptive Optics Systems II, edited by Brent L. Ellerbroek, Michael Hart, Norbert Hubin, Peter L. Wizinowich,
Proc. of SPIE Vol. 7736, 77362A · © 2010 SPIE · CCC code: 0277-786X/10/$18 · doi: 10.1117/12.858270

The GPI instrument consists of a new AO system,[2,10] an optimized coronagraph Apodised Pupil Lyot Corornagraph[11] (APLC), a calibration unit[9] (Cal). The combination of these three subsystems will yield a high quality PSF, that features deep contrast over the J, H and K bands. The observations will be carried out using an lens-let based Integral Field Spectrograph (IFS), thus providing low resolution spectroscopy of the discovered self-luminous Jupiter analogs. The calibration system is composed of two separate cameras, a low order wavefront sensor (LOWFS) and a high order one (HOWFS). The LOWFS re-images the core of the PSF into a pupil and measures the slopes of this wavefront using a Shack-Hartmann sensor. This low-order component is captured using an annular focal plane mask.[12] Part of this PSF core is also sent, via a beamsplitter and a spatial filter, to a phase shifting mirror that creates a reference arm for the HOWFS. Part of the coronagraphic Lyot plane is recombined with this phase shifted reference in order to measure the post coronagraphic electrical field distribution. This measurement is similar in principle to regular phase shifting interferometry, except that it occurs after a coronagraph where the beam amplitude is very faint and the low orders have been filtered out. The interferogram is acquired using a Lyot plane infrared camera whose operations are independent of the science exposures. This provides a non-intrusive wavefront sensing method. While the Signal to Noise Ratio (SNR) obtained using the interferometric HOWFS is similar to the one yielded using focal plane wavefront sensing methods,[13] its independent operations that enable PSF stability during the course of a science observation.

Wavefront correction is a non-linear process[14] that is generally solved using an iterative scheme: the loop is closed by applying each phase estimate to the Deformable Mirror (DM) that is located before the coronagraph, and then proceeding to a new wavefront measurement. Since the GPI Cal system operates in closed loop, estimation errors that correspond to a scaling of the actual wavefront only influence the convergence rate of the correction algorithm and do not have an impact the ability of the HOWFS to provide a high contrast PSF.[15] However the measurement is based on a model of the HOWFS and in particular it assumes that the interferometer operates with zero path length difference between the two arm. If this assumption does not hold then a bias will be introduced in the phase estimate. Depending the performance of the coronagraph and the magnitude of the incident wavefront errors, this bias can affect in certain cases the success of the convergence of the non linear iterative algorithm. The purpose of this paper is to identify the configurations of the GPI instrument for which differential path errors in the HOWFS perturb the nominal mid to high spatial frequencies control scheme, and to introduce solutions that alleviate this problem. In a first section we present the theoretical framework of this study. We then show how in particular differential path errors are the source of both gain and bias errors in the Cal estimate. We introduce two refinements of the currently envisioned sensing algorithms, respectively based on relative and absolute wavefront measurements, that allow to retrieve the nominal performance of the Calibration system in its non-nominal operations. We in a third part we use numerical simulations based on and efficient coronagraphic propagation code to quantify the performance of each approach. Finally we present an experimental validation of the apparatus that has been built at JPL.

## 2. POST CORNAGRAPHIC WAVEFRONT SENSING WITH A CAL SYSTEM

### 2.1. The GPI calibration system open loop

The GPI calibration system is composed of two wavefront sensors.[9] The low order sensor uses the core of the PSF, rejected by the coronagraph, in order to estimate the first 15 zernike modes of the incident wavefront. The PSF core is re-imaged to a pupil and its wavefront slopes are measured using a Shack Hartmann sensor. Guyon et.al[16] devised and tested a similar concept, namely measuring low order errors from the light rejected by the coronagraph, using a defocus based wavefront sensor. The SNR properties of a defocus based estimation scheme are superior to the Shack Hartmann solution, and makes it more suitable for small aperture space based exo-planet observatories. However the GPI architecture is sufficient to reach the precision level requirement for ground based eight meter class telescope. We direct the reader to a communication in the present proceedings for a detailed quantification of the performances of the GPI LOWFS. The architecture of the whole Cal system is illustrated on Fig. 1. The high-order wavefront sensor that is the focus of the present paper is based on a post coronagraphic phase-stepping interferometer. The first beam splitter of this interferometer is the focal plane mask, that consists on an annulus reflecting the outer part of the PSF towards the Lyot plane of the coronagraph

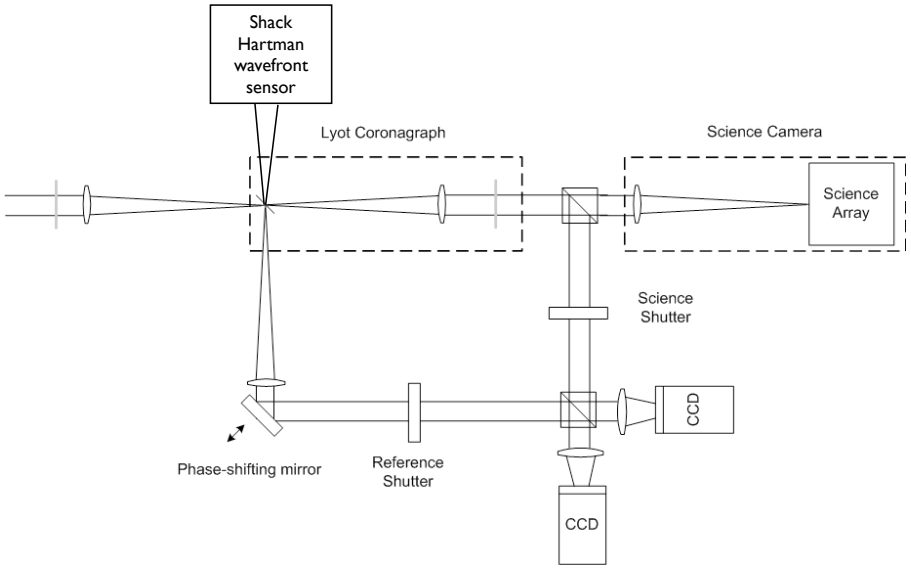


**Figure 1.** Bloc diagram of the GPI calibration system. The LOWFS measures the low order components of the entrance wavefront directly from the PSF core. The HOWFS consist on a Lyot plane phase shifting interferometer that estimates the mid to high spatial frequency components of the field at the DM.

and transmits the core of the PSF to both the LOWFS and a reference arm. We write the incident electric field as:

$$E_{in}(x,y) = A(r)(1+s(x,y))e^{i(\phi(x,y)-\phi^{(\lambda)}_{DM}(x,y))} \tag{1}$$

where $A(r)$ is the apodising screen profile of the Apodized Pupil Lyot Coronagraph[11] (APLC), $s(x,y)$ is term corresponds to the reflectivity errors in the optics, scintillation and phased induced amplitude amplitude errors.[17] Here we assume that $s$ is negligible.[4] $\phi$ stands for the phase errors and depends on the wavelength $\phi = \phi^{(\lambda)} = \frac{2\pi\lambda_0}{\lambda}\phi^{(0)}$, where $\lambda_0$ is the central wavelength in the bandwidth of interest. We control the wavefront with the twitter mirror of the AO system, that creates a wavefront deformation $\phi_{DM}$. The field in the reference arm, propagated through both a focal plane mask and a spatial filter:

$$E_{ref}(x,y) = E_{in}(x,y) \star \hat{m_C}(x,y) \star \hat{m_P}(x,y) \tag{2}$$

where $\hat{m_C}(x,y)$ is the Fourier Transform of the hole in the focal plane mask, and $\hat{m_P}(x,y)$ the Fourier Transform of the spatial filtering pinhole in the reference arm, and $\star$ stands of the convolution operator. Since this pinhole is smaller than the focal plane mask, it dominates the convolution. Its size has been chosen for an optimal tradeoff between the total flux in the reference arm and the amount of low order error transmitted. Simulations showed that a 5 $\mu$m diameter for the spatial filter will couple a reasonable amount of light wile ensuring a sufficiently flat reference phase. Thus here we assume that the reference field only exhibits an amplitude profile, $R(x,y)$ with flat phase, that is phase shifted:

$$E_{ref}(x,y) = R(x,y)e^{i\frac{2\pi}{\lambda}\lambda_0\Delta z} \tag{3}$$

with the stepping scheme: $\Delta z = 0, 1/4, 1/2, 3/4$. A pupil based beam re-combiner adds the field resulting from each one of these phase steps with the a fraction of field in the science arm that is sent to the HOWFS camera through a pick-off beamsplitter:

$$E_{sci}(x,y) = \mathcal{C}[A(r)] + i\mathcal{C}[(A(r)sin(\phi(x,y))] + \mathcal{C}[(A(r)(cos(\phi(x,y)) - 1)] \tag{4}$$

where $\mathcal{C}[\cdot]$ stands for the coronagraph operator. Since the coronagraph also acts as a spatial filter, these three terms can be simplified as:

$$\mathcal{C}[A(r)] \quad = \quad A^{(\lambda)}_C(r) \tag{5}$$

$$\mathcal{C}[(A(r)sin(\phi(x,y))] = c^{(\lambda)}(x,y)A(r)sin(\phi^{\lambda}(x,y)) \quad (6)$$

$$\mathcal{C}[(A(r)(cos(\phi(x,y))-1))] = d^{(\lambda)}(x,y)A(r)(cos(\phi^{\lambda}(x,y))-1). \quad (7)$$

$A_C^{\lambda}(r)$ is the response of the coronagraph at the considered wavelength. Each incident spatial frequencies is attenuated by the coronagraph according to a transfer function that follows the profile of a high pass filter with the focal plane mask radius as cutoff frequency.[15] Then, the combined interferogram at one wavelength is then given by:

$$I_{\Delta z}(x,y) = |E_{sci}|^2 + |E_{ref}|^2 + 2*|E_{ref}|*(A_C^{\lambda}(r) + d^{(\lambda)}(x,y)A(r)(cos(\phi^{\lambda}(x,y))-1))cos(\frac{2\pi}{\lambda}\lambda_0\Delta z) \quad (8)$$

$$+ \quad 2*c^{(\lambda)}(x,y)A(r)sin(\phi^{\lambda}(x,y))sin(\frac{2\pi}{\lambda}\lambda_0\Delta z). \quad (9)$$

This interferogram exhibits as a constant pedestal and term proportional to the real and imaginary part of the field in the science plane that is modulated by the phase-shifting. The modulation we chose for the GPI HOWFS, $\Delta z = 0, 1/4, 1/2, 3/4$, is equivalent to projecting the field in the science arm on symmetric and anti-symmetric kernels. Using differences between two phase shifted states and re- normalizing by the pedestal yields the following monochromatic Cal estimates:

$$\phi_{HOWFS} = \frac{I_{1/4} - I_{3/4}}{4A(r)|E_{ref}|} = c(x,y)^{\lambda}sin(\phi^{\lambda}(x,y)) \simeq \phi^{\lambda}(x,y) \quad (10)$$

$$s_{HOWFS} = \frac{I_0 - I_{1/2}}{4A(r)|E_{ref}|} = \frac{A_C(r)}{A(r)} + d(x,y)^{\lambda}(cos(\phi^{\lambda}(x,y))-1)) \simeq \frac{A_C(r)}{A(r)} + \frac{1}{2}(\phi^{\lambda}(x,y)))^2 \quad (11)$$

$$(12)$$

Eqs. 10 11 shows that, monochromatically, the HOWFS measures a quantity that is proportional to the input phase, and a quantity that is proportional to the real part of the field in the Lyot plane, which is equal to the coronagraphic leakage plus the second order of the phase expansion.[18,19] The nominal HOWFS operating mode, that is the focus of this paper, only uses the information contained in $\phi_{HOWFS}$ to control the DM. We find that even in the monochromatic case the Cal estimate only provides a measurement of the input phase that is modulated by a gain due to the partial filtering of low to mid spatial frequencies by the APLC. This effect will be larger in the broadband case since integrating Eq. 10 will superimpose a visibility envelope to the phase shifting response. While this chromatic effect could be alleviated using a $\Delta z = -1/4, 0, 1/4, 1/2$ phase shifting scheme, we show next that such a modification is not necessary in a closed loop correction scheme. Fig. 2 illustrates the result shown in Eq. 10, namely how sensing the imaginary part of the Lyot plane field is equivalent to measuring the incident phase.[20]

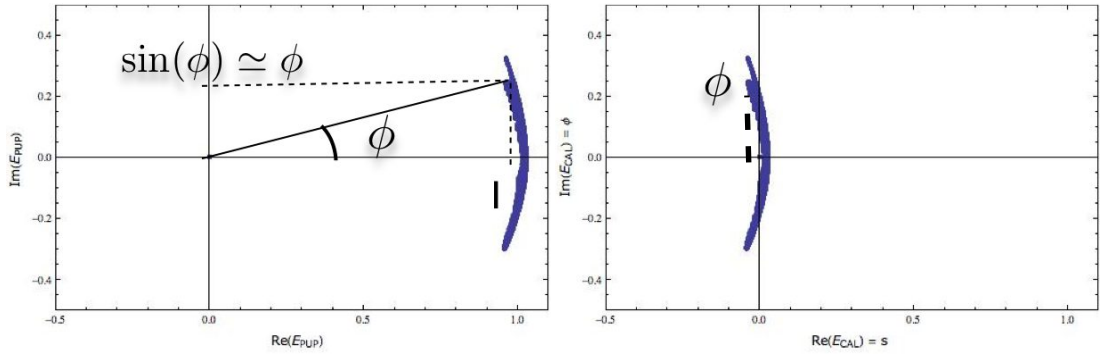


**Figure 2.** Illustration of our post coronagraphic wavefront sensing strategy: the imaginary part of the field in the Lyot plane is approximately equal to the incoming phase errors.

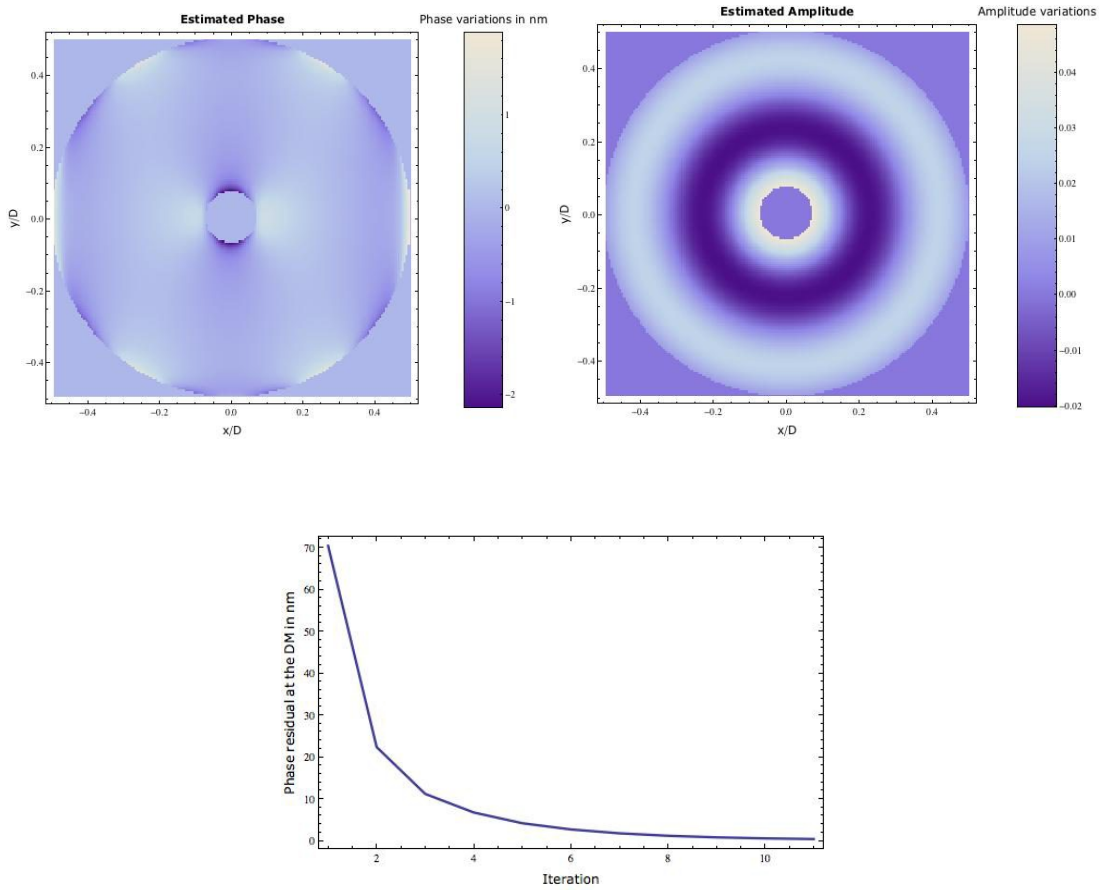


**Figure 3.** Top: simulated phase and amplitude residuals of the GPI HOWFS after ten iterations. Bottom: rms of the phase residual at the DM as a function of iteration. The coronagraph is optimized for H band observations. There are no differential path errors between the two arms of the Cal interferometer

## 2.2. Closed loop operations

Ultimately we are interested in the closed loop operation of the Cal system, thus the metric in we will use in this manuscript is the residual phase after a series of iterations. We adopt a sensing strategy that is in accordance Mugnier et.al[21] who suggests to only carry out quasi static-speckles measurements after a time average of the atmospheric residuals. Thus we will acquire a new Cal estimate every six seconds. The requirement for the HOWFS is to yield a 1 nm phase residual after a minute, as consequence the goal of this paper is to provide sensing strategies that will lead to a 1 nm rms wavefront error at the DM after ten iterations. We quantify the impact of bandwidth using numerical integrations in the H band, which is corresponds to the wavelength coverage of the HOWFS detector. We carry out simulations in two case: when the coronagraph is optimized of H band observations and when the coronagraph is optimized for J band observations. In the case of a J band optimized corornagraph the response seen by the Cal system, $A_C^{(\lambda)}(r)$, exhibits a high amplitude leak since the HOWFS camera acquires interferograms in the H band. In the case where there are no differential phase errors between the two arms of the interferometer, this chromatic leak does not have an influence on the convergence of the closed loop phase calibration loop, as seen in Fig. 3 and Fig. 4, where the 1 nm rms residual phase

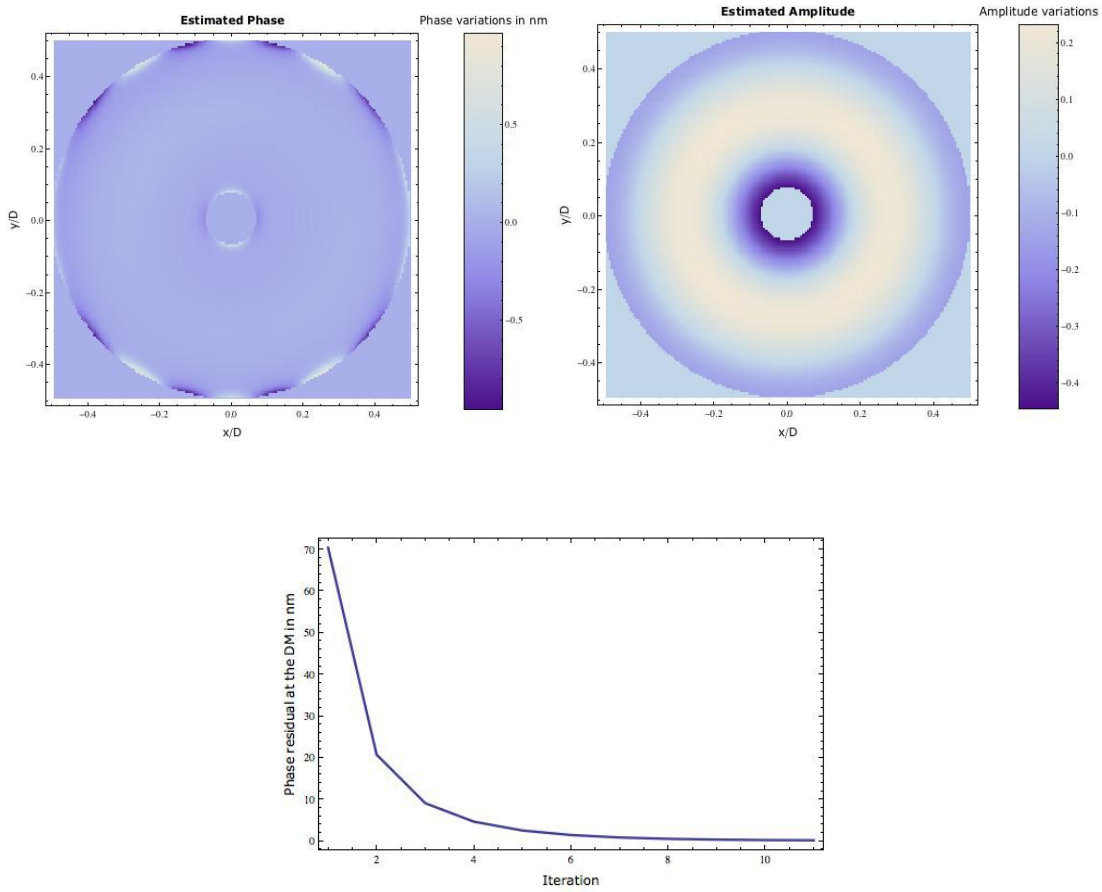


**Figure 4.** Top: simulated phase and amplitude residuals of the GPI HOWFS after ten iterations. Bottom: rms of the phase residual at the DM as a function of iteration. The coronagraph is optimized for J band observations. There are no differential path errors between the two arms of the Cal interferometer

requirement is achieved after 10 iterations in both configurations. This is due to the fact that a gain error in the phase retrieval only impacts the convergence rate and does not have an influence on overall result. In the next section we explore the case of differential path errors.

## 3. IMPACT OF DIFFERENTIAL PHASE ERRORS

### 3.1. Statement of the problem

The presence of differential path length errors between the two arms of the interferometer can potentially hamper the convergence of the correction algorithm. Such wavefront corrugations can arise from polishing errors in the optics, or from themo-mechanical drifts that slowly modify the alignment of the apparatus. The magnitude of some of these effects will only be quantified once the instrument is located in its nominal environment at the telescope. The objective of this paper is to predict the impact of mild to severe differential path errors for several HOWFS operation modes, identify the regimes in which the basic closed loop approach presented above does not yield the required performance, and propose alternate strategies to accommodate for these extreme cases.

In the presence of differential path length errors, the equation for the visibilities can be written as

$$I_{\Delta z}(x,y) = |E_{sci}|^2 + |E_{ref}|^2 + 2 * |E_{ref}| * (A_C(r) + d^{(\lambda)}(x,y)A(r)(cos(\phi^{\lambda}(x,y)) - 1))cos(\frac{2\pi}{\lambda}\lambda_0\Delta z - \theta) \quad (13)$$

$$+ \quad 2 * c^{(\lambda)}(x,y)A(r)sin(\phi^{\lambda}(x,y) - \theta)sin(\frac{2\pi}{\lambda}\lambda_0\Delta z). \quad (14)$$

where $\theta$ stands for the accumulated differential path wavefront error. Then the Cal estimate becomes:

$$\phi_{HOWFS} = \frac{I_{1/4} - I_{3/4}}{4A(r)|E_{ref}|} \simeq c^{(\lambda)}(x,y)\phi^{\lambda}(x,y)\cos\theta + d^{(\lambda)}(x,y)(\frac{A_C(r)}{A(r)} + \frac{1}{2}(\phi^{\lambda}(x,y)))^2)\sin\theta \quad (15)$$

$$s_{HOWFS} = \frac{I_0 - I_{1/2}}{4A(r)|E_{ref}|} \simeq -c^{(\lambda)}(x,y)\phi^{\lambda}(x,y)\sin\theta + d^{(\lambda)}(x,y)(\frac{A_C(r)}{A(r)} + \frac{1}{2}(\phi^{\lambda}(x,y)))^2)\cos\theta \quad (16)$$

$$(17)$$

Thus the HOWFS estimate exhibits a bias that scales with, $A_C^{\lambda}(r)$, $\phi^2$ and $\theta$. Such a bias can have a strong impact on the convergence of the closed loop phase controller. Since it will drive the phase at the DM to value that is non zero, this bias can prevent convergence towards a dark enough speckle field, and can also hamper the stability during the course of an observation. Fig. 5 illustrates how the complex distribution of the filed in the Lyot plane is rotated when $\theta \neq 0$. The magnitude of the bias on the phase estimate depends on the coronagraphic response

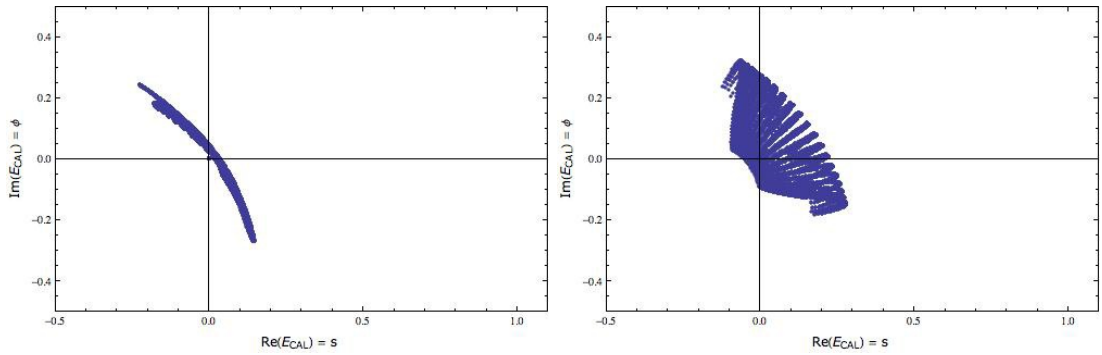


**Figure 5.** Argan diagram of the complex plane distribution of the Cal estimate in the presence of differential path errors. Left: case of a coronagraph optimized of H band observations. Right: case of a coronagraph optimized of J band observations.

as shown on Fig. 6, the HOWFS measures the vertical dashed vector while the iterative scheme assumes that it is measuring the dotted phasors. When the coronagraph is optimized for H band observations, the projection of the coronagraphic response the imaginary axis leads to a small bias. Fig. 7 illustrates the closed loop performances of the HOWFS in this case, with a $\lambda/10$ tilt differential phase errors and a 80 nm rms input wavefront error. The Cal system drives the phase at the DM to a biased value that corresponds to the product of the tilt with the coronagraphic response. Since in this case $A_C^{(\lambda)}(r)$ is of the order of a percent, its projection onto the sensed phased is smaller than the 1 nm requirement. However when the science operations are carried out in the J band, with a J band optimized coronagraph, then the static response is much larger as seen from the HOWFS camera, in the H band. As shown on the left panel of Fig. 6, this leads to a much larger error on the estimated phase. This bias impacts the convergence of the iterative correction, limited to 9 nm rms. Such a poor performance level will drastically affect the PSF quality, rendering the observations of young Jupiter very difficult. Next we propose two solutions to mitigate this problem.

### 3.2. Biais supression, relative wavefront sensing

A first alternative consists on measuring a priori the bias in the estimate that is created by the cross talk between the off-wavelength amplitude response of the coronagraph and the differential path errors. This solution assumes

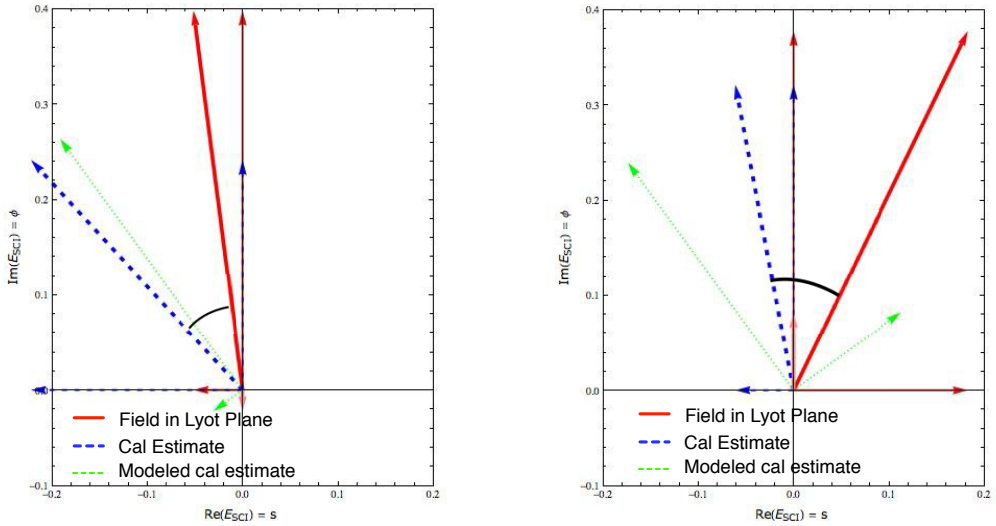


**Figure 6.** Detailed Argan diagram of spatial location in the Lyot plane in the presence of differential path errors. Left: case of a coronagraph optimized of H band observations. Right: case of a coronagraph optimized of H band observations. The bias due to the differential path errors is significantly larger in the off-wavelength case.

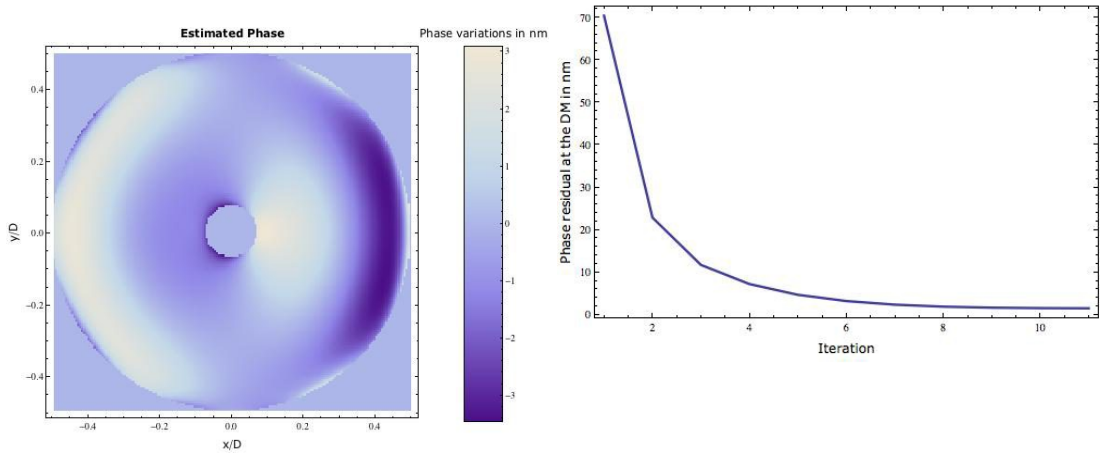


**Figure 7.** Left: simulated phase residuals of the GPI HOWFS after ten iterations. Right: rms of the phase residual at the DM as a function of iteration. The coronagraph is optimized for H band observations. The differential path errors between the two arms of the Cal interferometer is a $\lambda/10$ tilt. In this case the final phase residual at the DM after convergence is 1 nm

a preliminary calibration procedure that flattens the phase at the plane of the DM independently of any HOWFS measurement. Such methods are discussed below. For now, if we assume that $\phi = 0$ then we can carry out a first Cal system estimate:

$$\phi^{(0)}_{HOWFS} \quad = \quad d^{(\lambda)}(x,y)(\frac{A_C(r)}{A(r)} + \frac{1}{2}(\phi^{\lambda}(x,y)))^2)\sin\theta \tag{18}$$

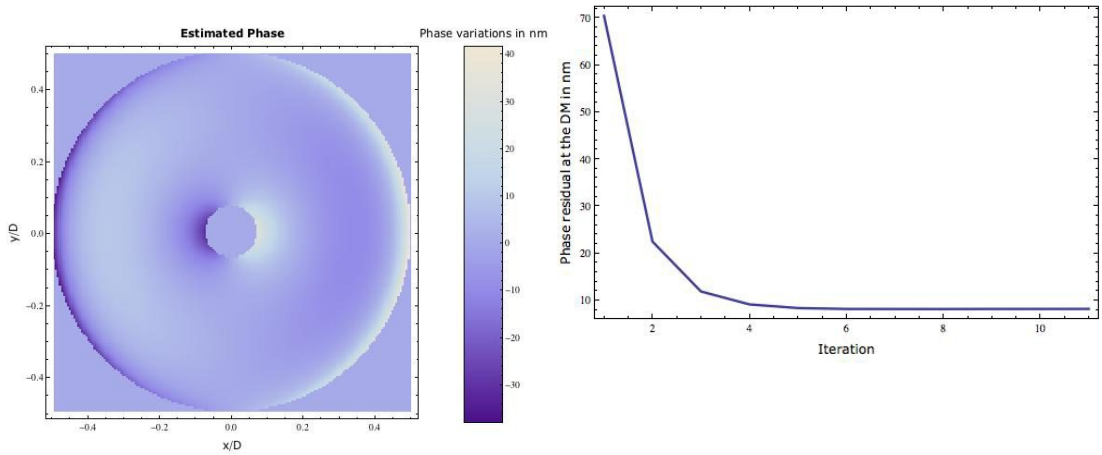


**Figure 8.** Left: simulated phase residuals of the GPI HOWFS after ten iterations. Right: rms of the phase residual at the DM as a function of iteration. The coronagraph is optimized for H band observations. The differential path errors between the two arms of the Cal interferometer is a $\lambda/10$ tilt. The nominal iterative algorithm converges to a residual that is 9 nm rms.

$$s^{(0)}_{HOWFS} = d^{(\lambda)}(x,y)(\frac{A_C(r)}{A(r)} + \frac{1}{2}(\phi^{\lambda}(x,y)))^2)\cos\theta. \tag{19}$$

$$\tag{20}$$

If we assume that the differential phase is static, and that $\phi^2 \ll 1$ is negligible, then we can use this estimate as a reference point for our algorithm:

$$\phi_{HOWFS} = \frac{I_{1/4} - I_{3/4}}{4A(r)|E_{ref}|} - \phi^{(0)}_{HOWFS} \tag{21}$$

and thus subtract this bias from the HOWFS estimate. The crucial stage in this scheme is to obtain a measurement of the incident phase that is accurate enough to measure the bias inherent to the Cal system. A first possibility would be to use phase diversity focal plane measurements.[22,23] However such a method would only provide a phase estimate for the field in the Lyot plane of the coronagraph, which would need to be back propagated to the entrance pupil. Such a problem is ill posed and inverting it without amplifying the measurement noise is a delicate exercise. Another option, that alleviates this inversion issue, would be to use a Lyot plane based wavefront estimate based on dithering the DM with defocus modes.[24] In order to use this method a detector would be needed in the actual science path of the GPI instrument, since if it is carried out using the HOWFS camera, the phase errors in the interferometer science arm will bias the measurement. A final, and more suitable option consists on using image plane based speckle nulling approaches.[14,25,26] We direct the reader towards a paper by Thomas et.al in these proceedings that presents experimental dark holes at the $5 \times 10^{-8}$ obtained using the GPI coronagraph architecture. While the phase is not flattened by such algorithms, they ensure a very high contrast PSF in the region of the image where one expects to find faint companions. The Cal system bias, $\phi^{(0)}_{HOWFS}$, can then be measured when the DM offset is controlled in a dark hole configuration. In this regime, the Cal system will provide a relative phase measurement and deliver wavefront stability to the GPI instrument. The main limitation of this scheme is that when the DM is commanded using speckle nulling algorithms the incident wavefront it not flat, in particular it contains large high spatial frequency deformations that correspond to speckles outside of the image plane dark hole. While these fourier components interfere destructively in the region of interest of the image plane, they do not respect the $\phi^2 \ll 1$ condition. They can potentially fold into

relatively large mid spatial frequency amplitude errors that will act as DM dependent amplitude errors in the science arm of the cal system and affect the bias of the phase stepping reconstruction algorithm from iteration to iteration. As an alternative we present next an absolute wavefront measurement procedure.

### 3.3. Absolute de-rotation

In order to obtain an absolute estimate we need to measure the differential phase angle $\theta(x, y)$ and use it to de-rotate the phasors illustrated in Fig. 6. The angle of this de-rotation ought to correspond to the differential phase between the two arms of the interferometer. Measuring this angle can be done in two fashions. First, at each iteration, we can can use the phase stepping algorithm on the light rejected by the coronagraph, located in the secondary shadow or within an outside annulus at the edge of the Lyot stop. In the absence of differential phase errors the HOWFS measurement in these regions ought to be purely real, and thus any detected imaginary component is proportional to $\theta(x, y)$. Because these zones do not cover the region of interest of the HOWFS only the first few zernikes of differential path can be retrieved using this method and extrapolated to the region inside the Lyot stop. Full retrieval of the differential path errors can be obtained using the following initial calibration approach:

- For a given arbitrary incident wavefront, use the HOWFS to measure a Cal estimate $\hat{E}_{HOWFS}$
- Acquire a series of in focus and defocused images with the science camera, $I_{SCI}^{(0)}$, $I_{SCI}^{(+m\lambda)}$, $I_{SCI}^{(-m\lambda)}$, where $m$ is the defocus in waves
- Use a phase diversity retrieval algorithm to retrieve the actual field at the Lyot plane of the science path. The amplitude constraint for this algorithm is $|\hat{E}_{HOWFS}|$, and the starting point for the phase is $arg(\hat{E}_{HOWFS})$. Assuming that the differential errors are smaller than a wave, and that $m$ is well chosen,[27] these conditions ensure convergence towards the true phase in the Lyot plane of the science channel.

$$E_{Retrieved} = GS(I_{SCI}^{(0)}, I_{SCI}^{(+m\lambda)}, I_{SCI}^{(-m\lambda)}, |\hat{E}_{HOWFS}|, arg(\hat{E}_{HOWFS})) \tag{22}$$

  where $GS$ stands for the iterative Gerchberg Saxon algorithm.[22]

- Retrieve the differential errors by comparing the retrieved field in the Lyot plane with the estimate one:

$$\theta_{retrieved} = arg(\hat{E}_{HOWFS}) - arg(E_{Retrieved}) \tag{23}$$

Note that this method is fundamentally different from the phase retrieval approach suggested earlier, since it does not require to de-convolve the coronagraphic response from the result obtained using the defocus diversity algorithm. Here we do not require to flatten the incident phase since the purpose of the phase diversity measurement is only to calibrate the differential phase by comparing the HOWFS estimate with the Lyot field distribution in the science path. Using $\theta_{retrieved}$ we then de-rotate the cal estimate, and thus for each interferometric measurement we compute the true Cal estimate as follows:

$$\phi_{HOWFS} = \frac{I_{1/4} - I_{3/4}}{4A(r)|E_{ref}|}\cos(\theta_{retrieved}) - \frac{I_0 - I_{1/2}}{4A(r)|E_{ref}|}\sin(\theta_{retrieved}) \tag{24}$$

This is equivalent of projecting the HOWFS estimate on the dotted lines in Fig. 6 instead of projecting on the real and imaginary axis. This phase retrieval approach to measure the differential phase in the interferometer can only be carried out at the beginning of each observation, which is a drawback compared to the low-order absolute de-rotation based on the secondary shadow. However we do not expect the mid-spatial frequency components of the differential phase to be time varying above the nanometer level. Thus combining a pre-observing high order phase retrieval and on the fly low order calibration will provide a robust method to carry out Cal estimate field de-rotation, and thus lead to an absolute Cal measurement. This method present a tremendous advantage over the relative estimation scheme since it is non sensitive to the magnitude of the incoming aberration. Next we present numerical simulations that identify the performance of both relative and absolute phase estimate.

## 4. NUMERICAL RESULTS

We carried out a series of simulation assuming incident errors that follow a ripple profile, and differential phase errors that behave as a $1/f^2$ power spectrum. We varied the spatial frequency of the input phase ripple as well as its magnitude and the magnitude of the differential path error. We adopted an optimistic case for the relative estimation scheme and assumed that one was capable of perfectly flattening the incident phase in order to measure the bias. For the simulation of the absolute measurement scheme we implemented the defocus diversity method. Our calculations were carried out in the worse case configuration where the coronagraph is optimized of J band observations and the Cal system acquires H band interferograms.

Results are shown on Figs. 9, 10 and 9. For 8 and 12 cycles per aperture there exists an extreme regime for which the relative phase measurement strategy yields a residual above the 1 nm requirement. In this extreme case, the absolute sensing scheme provides a robust alternate solution. In the case of 4 cycles a significant part of the incident wave is filtered by the coronagraph, thus the contribution of $\phi^2$ in the Lyot plane is not as significant, leading to efficient relative calibration over the whole range of values simulated here. Because of the value of $m$ chosen in our simulations, close to one of the blind spatial frequencies of the phase diversity algorithm,[27] the phase diversity required for the absolute calibration in the case of 4 cycles per aperture is less accurate. This leads to slightly poorer performance of the absolute calibration method in the case of a low spatial frequency. However in practice the incident wavefronts are a sum of a continuum of ripples, and this effect should be small.

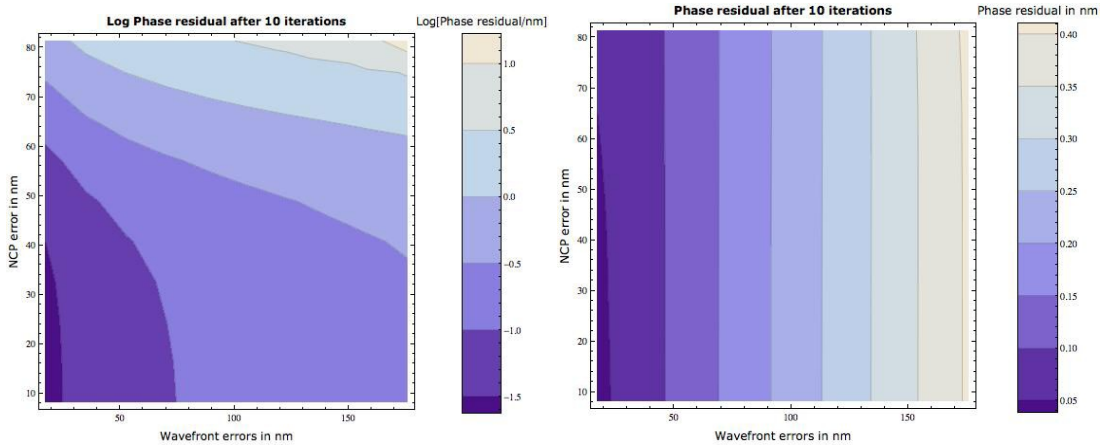


**Figure 9.** Left: Relative estimation method, contours plot of the residual rms wavefront errors at the DM after 10 iterations as a function of the magnitudes of the incoming errors and differential path length. Right: Absolute estimation method, contours plot of the residual rms wavefront errors at the DM after 10 iterations as a function of the magnitudes of the incoming errors and differential path length. The coronagraph is optimized for J band observations and the spatial frequency of the incident ripple is 8 cycles per aperture. Note that the right hand panel is shown in a logarithmic scale: there exists a regime where the 1 nm requirement is not met using the relative measurement method.

The results are shown on Fig. 9, Fig. 10 and Fig. 11 for incident ripples of respective spatial frequencies 8, 4 and 12 cycles per aperture. In most cases both methods yield a residual error after 10 iterations that are below the 1 nm requirement. As predicted, the absolute measurement approach is much less sensitive to magnitude of the input errors. While the nominal GPI scheme is relative measurements, the absolute method provides an efficient contingency methods in the extreme regime of large wavefront errors, as see on the top right region of the two panels on Fig. 9. Future plans include a careful study of the relative method when the bias is measured using a speckle nulling DM setting, for which quantifying the impact on the HOFWS bias of the frequency folding terms in $\phi^2$ is crucial.

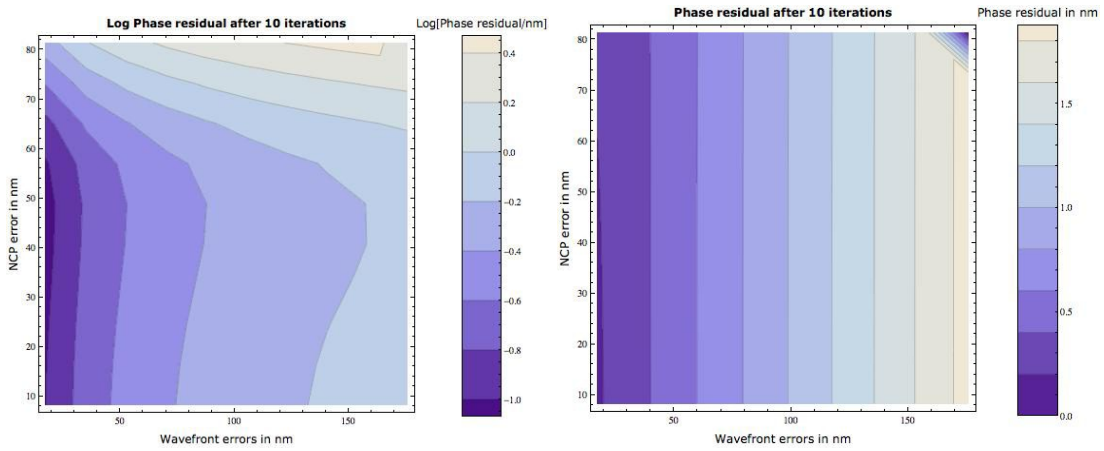


**Figure 10.** Left: Relative estimation method, contours plot of the residual rms wavefront errors at the DM after 10 iterations as a function of the magnitudes of the incoming errors and differential path length. Right: Absolute estimation method, contours plot of the residual rms wavefront errors at the DM after 10 iterations as a function of the magnitudes of the incoming errors and differential path length. The coronagraph is optimized for J band observations and the spatial frequency of the incident ripple is 4 cycles per aperture

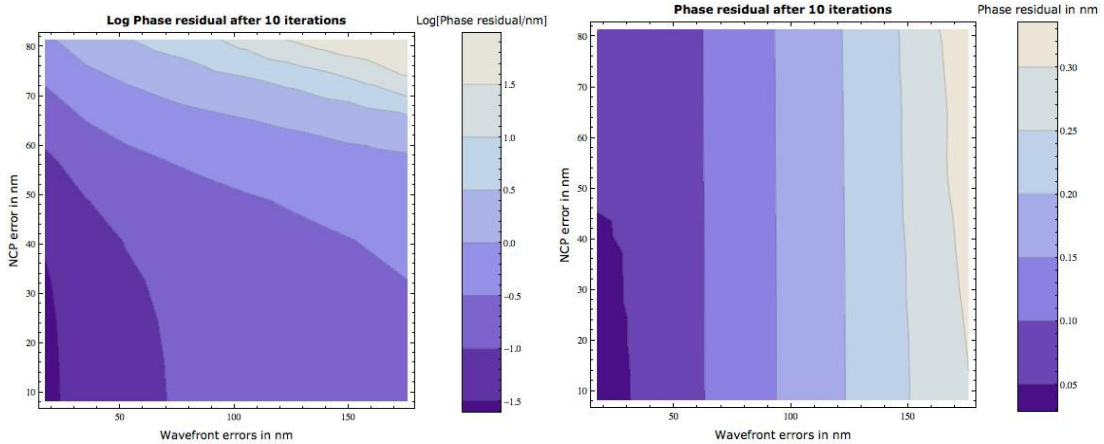


**Figure 11.** Left: Relative estimation method, contours plot of the residual rms wavefront errors at the DM after 10 iterations as a function of the magnitudes of the incoming errors and differential path length. Right: Absolute estimation method, contours plot of the residual rms wavefront errors at the DM after 10 iterations as a function of the magnitudes of the incoming errors and differential path length. The coronagraph is optimized for J band observations and the spatial frequency of the incident ripple is 12 cycles per aperture. Note that the right hand panel is shown in a logarithmic scale: there exists a regime where the 1 nm requirement is not met using the relative measurement method.

## 5. GPI TESTBED

In this section we briefly present results obtained using the final instrument, that has been assembled over the past few months at JPL, see Fig. 12. Because the Cal system will be tested in closed loop operation only during the integration and test phase of the GPI project, we devised preliminary a method to quantify the open loop performance of the HOWFS. We inserted a known wavefront error at the pupil plane for the coronagraph. This fiducial error consists on a microscope slide whose wavefront was calibrated using a infra-red zygo interferometer. We then used this preliminary measurement to compute the expected HOWFS estimated using a numerical propagator[28] through the APLC can the Cal interferometer. We compared this simulated measurement of the the actual result yielded by the instrument. Thus the metric of our open loop validation method is based

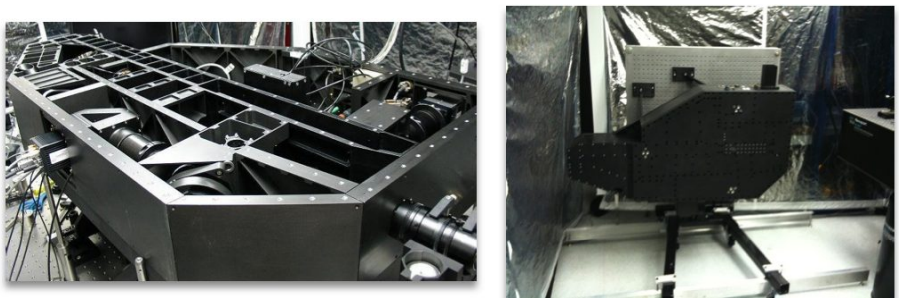

**Figure 12.** Final assembly of the GPI Calibration system

on phase retrieval at the Lyot plane of the coronagraph, the absence of a DM in our testbed preventing us from projecting the estimate back to the entrance pupil and iterate. Our first series of measurements lead to a 8 nm rms wavefront error that was dominated by cross talk between estimated amplitude and phase. The spatial structure of this cross talk followed a ramp profile, and we thus diagnosed a tilt differential path error between the two arms of the interferometer. We then proceeded to measure this error and de-rotated the Cal estimate as presented above. Finally we re-aligned the apparatus and went through another set of phase stepping measurements. The residual errors of this two methods were consistent, at the 4.5 nm level, these results are illustrated on Fig. 13. Disentangling the bias errors from gain errors contained in this absolute phase residual requires closed loop operations and will be one of our first item of action during the integration and test phase of the GPI instrument.

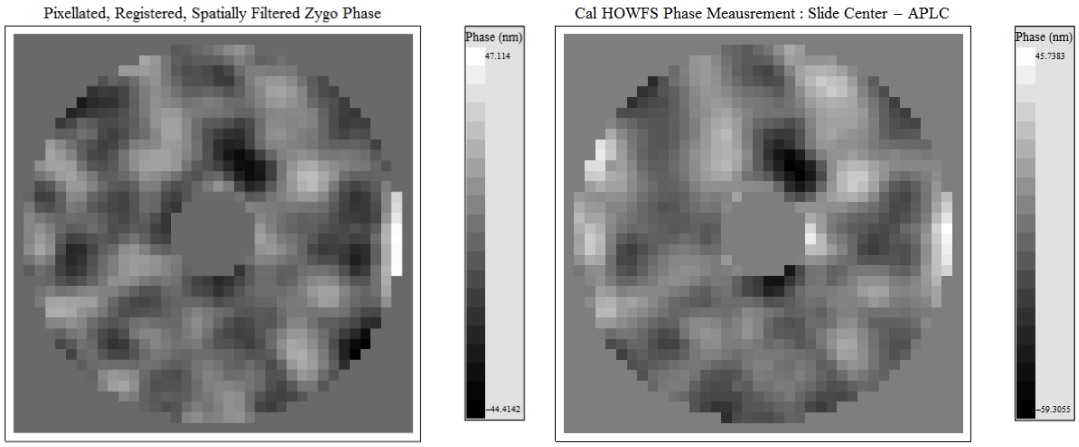


**Figure 13.** Left: predicted HOWFS phase estimate using numerical propagation of a know microscope slide phase screen. Right: HOWFS estimate obtained using the GPI Cal system at JPL. The rms error between the two phase maps is 4.5 nm.

## 6. CONCLUSION

In this paper we delved into the intricacies of the GPI Calibration interferometer. Such an apparatus is different from classical phase shifting approaches because it is tightly packaged around a coronagraph an the nominal wavefront sensing algorithms assume that the coronagraph operates at high starlight rejection levels. Because the GPI HOWFS camera only operates in the H band, there exist some modes, namely when observations are carried out in J and K band, where the statis coronagraphic response seen by the interferometer is not optimal. This yield to a bias on the phase estimate. Here we have shown two methods to alleviate this problem, relative

and absolute phase measurement. We simulated the performance of both algorithms for various parameters and show their complementarity. These modifications only consist on minimal changes to the baseline scheme. We then presented laboratory validation of the instrument that exhibits an open loop measurement with a phase residual smaller than 4 nm rms. This figure will decrease as the Cal system is integrated in a closed loop with the AO system and the DM. The simulations presented here provide insight towards the closed loop behavior of the HOWFS and will serve as guidelines for the both integration phase of GPI and future observations.

## Acknowledgements

The research described in this publication was carried out at the Jet Propulsion Laboratory, California Institute of Technology, under a contract with the National Aeronautics and Space Administration. The first author was supported by an appointment to the NASA Postdoctoral Program at the JPL, Caltech, administered by Oak Ridge Associated Universities through a contract with NASA.

## REFERENCES

1. Roddier, F., "The effects of atmospheric turbulence in optical astronomy," *Progress in Optics* **XIX**, 283–376 (1981).
2. Poyneer, L. A. and Véran, J.-P., "Optimal modal Fourier-transform wavefront control," *Journal of the Optical Society of America A* **22**, 1515–1526 (Aug. 2005).
3. Fusco, T., Petit, C., Rousset, G., Sauvage, J.-F., Dohlen, K., Mouillet, D., Charton, J., Baudoz, P., Kasper, M., Fedrigo, E., Rabou, P., Feautrier, P., Downing, M., Gigan, P., Conan, J.-M., Beuzit, J.-L., Hubin, N., Wildi, F., and Puget, P., "Design of the extreme AO system for SPHERE, the planet finder instrument of the VLT," in [*Advances in Adaptive Optics II. Edited by Ellerbroek, Brent L.; Bonaccini Calia, Domenico. Proceedings of the SPIE, Volume 6272, pp. 62720K (2006).*], *Presented at the Society of Photo-Optical Instrumentation Engineers (SPIE) Conference* **6272** (July 2006).
4. Graham, J. R., Macintosh, B., Doyon, R., Gavel, D., Larkin, J., Levine, M., Oppenheimer, B., Palmer, D., Saddlemyer, L., Sivaramakrishnan, A., Veran, J.-P., and Wallace, K., "Ground-Based Direct Detection of Exoplanets with the Gemini Planet Imager (GPI)," *ArXiv e-prints* **704** (Apr. 2007).
5. Serabyn, E., Mawet, D., and Burruss, R., "An image of an exoplanet separated by two diffraction beamwidths from a star," *Nature* **464**, 1018–1020 (Apr. 2010).
6. Sauvage, J.-F., Fusco, T., Rousset, G., and Petit, C., "Calibration and precompensation of noncommon path aberrations for extreme adaptive optics," *Journal of the Optical Society of America A* **24**, 2334–2346 (Aug. 2007).
7. Codona, J. L. and Angel, R., "Imaging Extrasolar Planets by Stellar Halo Suppression in Separately Corrected Color Bands," *ApJ Letters* **604**, L117–L120 (Apr. 2004).
8. Galicher, R., Baudoz, P., Rousset, G., Totems, J., and Mas, M., "Self-coherent camera as a focal plane wavefront sensor: simulations," *AAS* **509**, A31+ (Jan. 2010).
9. Wallace, J. K., Burruss, R., Pueyo, L., Soummer, R., Shelton, C., Bartos, R., Fregoso, F., Nemati, B., Best, P., and Angione, J., "The gemini planet imager calibration testbed," *Techniques and Instrumentation for Detection of Exoplanets IV* **7440**(1), 74400S, SPIE (2009).
10. Poyneer, L. A. and Macintosh, B., "Spatially filtered wave-front sensor for high-order adaptive optics," *Journal of the Optical Society of America A* **21**, 810–819 (May 2004).
11. Soummer, R., "Apodized Pupil Lyot Coronagraphs for Arbitrary Telescope Apertures," *ApJ Letters* **618**, L161–L164 (Jan. 2005).
12. Oppenheimer, B. R., Digby, A. P., Shara, M., Brenner, D., Newburgh, L., Makidon, R. B., Sivaramakrishnan, A., Soummer, R., Graham, J. R., Kalas, P., Perrin, M., Kuhn, J. R., Whitman, K., and Lloyd, J. P., "The Lyot Project: Toward Exoplanet and Circumstellar Disk Imaging and Spectroscopy," in [*Bulletin of the American Astronomical Society*], *Bulletin of the American Astronomical Society* **36**, 583–+ (Dec. 2003).
13. Guyon, O., "Limits of Adaptive Optics for High-Contrast Imaging," *ApJ* **629**, 592–614 (Aug. 2005).
14. Pueyo, L., Kay, J., Kasdin, N. J., Groff, T., McElwain, M., Give'on, A., and Belikov, R., "Optimal dark hole generation via two deformable mirrors with stroke minimization," *Appl. Opt.* **48**(32), 6296–6312 (2009).

15. Sivaramakrishnan, A., Soummer, R., Pueyo, L., Wallace, J. K., and Shao, M., "Sensing Phase Aberrations behind Lyot Coronagraphs," *ApJ* **688**, 701–708 (Nov. 2008).
16. Guyon, O., Matsuo, T., and Angel, R., "Coronagraphic Low-Order Wave-Front Sensor: Principle and Application to a Phase-Induced Amplitude Coronagraph," *ApJ* **693**, 75–84 (Mar. 2009).
17. Pueyo, L. and Kasdin, N. J., "Polychromatic Compensation of Propagated Aberrations for High-Contrast Imaging," *ApJ* **666**, 609–625 (Sept. 2007).
18. Perrin, M. D., Sivaramakrishnan, A., Makidon, R. B., Oppenheimer, B. R., and Graham, J. R., "The Structure of High Strehl Ratio Point-Spread Functions," *ApJ* **596**, 702–712 (Oct. 2003).
19. A.Give'On, Kasdin, N., Vanderbei, R., and Avitzour, Y., "On representing and correcting wavefront errors in high-contrast imaging systems," *JOSA* **23**, 1063–1073 (2006).
20. Soummer, R. and Ferrari, A., "The Strehl Ratio in Adaptive Optics Images: Statistics and Estimation," *ApJ Letters* **663**, L49–L52 (July 2007).
21. Mugnier, L. M., Sauvage, J., Fusco, T., Cornia, A., and Dandy, S., "On-Line Long-Exposure Phase Diversity: a Powerful Tool for Sensing Quasi-Static Aberrations of Extreme Adaptive Optics Imaging Systems," *Optics Express* **16**, 18406–+ (Oct. 2008).
22. Fienup, J. R., "Phase retrieval algorithms: a comparison," *Appl. Opt.* **21**(15), 2758–2769 (1982).
23. Guyon, O., "High Sensitivity Wavefront Sensing with a Nonlinear Curvature Wavefront Sensor," *PASP* **122**, 49–62 (Jan. 2010).
24. Green, J. J., Niessner, A. F., and Shaklan, S. B., "Post-coronagraph wavefront sensing using pupil imaging and phase-diversity," in [*Adaptive Optics: Analysis and Methods/Computational Optical Sensing and Imaging/Information Photonics/Signal Recovery and Synthesis Topical Meetings on CD-ROM*], *Adaptive Optics: Analysis and Methods/Computational Optical Sensing and Imaging/Information Photonics/Signal Recovery and Synthesis Topical Meetings on CD-ROM* , JTuB1, Optical Society of America (2005).
25. Bordé, P. J. and Traub, W. A., "High-Contrast Imaging from Space: Speckle Nulling in a Low-Aberration Regime," *ApJ* **638**, 488–498 (Feb. 2006).
26. Give'on, A., Belikov, R., Shaklan, S., and Kasdin, J., "Closed loop, dm diversity-based, wavefront correction algorithm for highcontrast imaging systems," *Opt. Express* **15**(19), 12338–12343 (2007).
27. Dean, B. H. and Bowers, C. W., "Diversity selection for phase-diverse phase retrieval," *J. Opt. Soc. Am. A* **20**(8), 1490–1504 (2003).
28. Soummer, R., Pueyo, L., Sivaramakrishnan, A., and Vanderbei, R. J., "Fast computation of Lyot-style coronagraph propagation," *ArXiv e-prints* **711** (Nov. 2007).